Materials Today Bio 29 (2024) 101334

Contents lists available at ScienceDirect

Materials Today Bio

journal homepage: www.journals.elsevier.com/materials-today-bio

A high-water retention, self-healing hydrogel thyroid model for surgical training

Liang Ma [a,b,1], Zhihao Zhu [b,1], Shijie Yu [a,b], Sidney Moses Amadi [c], Fei Zhao [d], Jing Zhang [a,**], Zhifei Wang [b,*]

[a] College of Materials Science and Engineering, Zhejiang University of Technology, Hangzhou, 310014, China
[b] General Surgery, Cancer Center, Department of Hernia Surgery, Zhejiang Provincial People's Hospital (Affiliated People's Hospital), Hangzhou Medical College, Hangzhou, Zhejiang, 310014, China
[c] International Education College, Zhejiang Chinese Medical University, Hangzhou, Zhejiang, 310000, China
[d] Center for General Practice Medicine, Department of Gastroenterology, Zhejiang Provincial People's Hospital (Affiliated People's Hospital), Hangzhou Medical College, Hangzhou, Zhejiang, 310014, China

ARTICLE INFO

Keywords:
High-water retention hydrogel
Self-healing
Thyroid simulation model
Surgical training

ABSTRACT

The evaluation of thyroid lesions through Fine-Needle Aspiration Biopsy (FNAB) is a common procedure that requires advanced hand manipulation skills. Conventional training models for this procedure lack essential features such as tactile sensation and the ability to repeat punctures similar to those of real organs. To improve the quality of training, we have developed a hydrogel thyroid model that possesses features such as high-water retention and self-healing properties. This model consists of polyvinyl alcohol (PVA), polyacrylic acid (PAA), and trehalose that enhance water retention. By utilizing indirect printing technology, this hydrogel-based thyroid model closely resembles those of porcine thyroid tissue in terms of compression modulus and friction coefficient, exhibiting exceptional conformability, flexibility, and a water retention rate of 94.7 % at 6 h. It also displays a thrust force range of 0–0.98 N during simulated puncture, closely approximating real FNAB operations. This model shows evidence that it effectively simulates thyroid tissue and can be utilized for repetitive FNAB training to enhance the proficiency of medical personnel. Our study focuses on introducing new possibilities for developing advanced materials training models to be utilized in the medical field.

1. Introduction

The utilization of tissue and organ models that accurately replicate anatomical features and tactile sensations is essential for effective preoperative planning, clinical medical training, teaching, and doctor-patient communication [1].Fine-needle aspiration biopsy (FNAB) is a commonly used procedure for assessing thyroid lesions but it requires a high level of precision and experience, especially in complex cases [2]. Despite advancements in imaging technology and artificial intelligence that enhance diagnostic accuracy and efficiency, these methods lack the ability to provide surgeons with realistic tactile feedback and elastic modulus measurements [3–5]. Traditional training methods involving animal tissues or preserved human tissues pose ethical, sustainability, and financial challenges [6]. Thus, developing training models that closely mimic real thyroid tissue is imperative to enhancing healthcare professionals' FNAB proficiency.

As physical objects, 3D-printed models serve as valuable tools for intuitive visualization in preoperative training [7]. However, the models currently available are primarily composed of silicone or resin materials, which lack the texture and modulus characteristics of real organs [8]. This limitation presents a challenge in achieving optimal outcomes with these models for preoperative training. Therefore, there is a need to identify and develop soft, slippery tissue-simulating materials that can accurately mimic the properties found in biological tissues. These materials should exhibit tissue-like softness and be designed to replicate the anatomical structure and mechanical properties of thyroid gland tissue.

The utilization of hydrogel materials as advanced biomaterials has garnered significant interest in recent years due to their unique physical

* Corresponding author.
** Corresponding author.
E-mail addresses: zhangjing@zjut.edu.cn (J. Zhang), wangzhifei1973@zju.edu.cn (Z. Wang).
[1] These authors contributed equally to this work.

https://doi.org/10.1016/j.mtbio.2024.101334
Received 6 June 2024; Received in revised form 7 November 2024; Accepted 7 November 2024
Available online 13 November 2024

and chemical properties. These materials possess remarkable elasticity, flexibility, and water retention capabilities, making them ideal candidates for mimicking biological tissues [9,10]. For instance, Tu [11] et al. successfully prepared PAMPS/PAA double-network (DN) hydrogels hybridized with TOCN and Py, demonstrating remarkable mechanical strength and electrical conductivity, showing high potential for various applications in the field of biomaterials. Liu [12] et al. successfully produced intricate and lifelike volumetric hydrogel organs through 3D printing by adjusting the composition of hydrogel materials, including kidneys, brains, hearts, livers, stomachs, lungs, tracheas, intestines, and complex vascular tissues. Similarly, Xu [13] et al. developed hydrogels with adjustable properties and achieved wet-slip hydrogel elastomers with customizable mechanical and physicochemical properties by varying component concentration and immersion time in ionic solutions. Leveraging 3D printing technology, designed and fabricated physical organ models with varying mechanical properties to closely simulate human tissues, facilitating surgical training in diverse scenarios. However, an inherent limitation of hydrogels is their tendency to lose moisture due to inevitable water evaporation [14], leading to water loss and hardening over time during surgical training, particularly in low-humidity environments. This phenomenon adversely impacts the training efficacy. Consequently, further research into enhancing the water retention capacity of hydrogels is crucial to prolong the service life of these models. Furthermore, fine-needle puncture procedures in thyroid surgeries do not involve any chemical reactions between surgical instruments and simulated models. This allows trainers to repeatedly practice on these models without compromising their structural integrity. Hence, there is a need for developing highly water-retaining and self-healing hydrogel materials with similar tactile sensations and moduli comparable to real thyroid tissues is expected to provide a low-cost, highly efficient training strategy.

Conventional strategies to mitigate the moisture depletion of hydrogels typically involve the incorporation of hygroscopic salts and organic solvents. These additives can impede water evaporation by increasing the enthalpy of vaporization or forming strong hydrogen bonds with water molecules [15,16]. However, while these methods improve water retention, they can negatively affect key properties such as mechanical strength, viscosity, gelation kinetics, and hydration capacity. Therefore, developing hydrogels that combine high water retention, desirable mechanical properties resembling soft biological tissues, and rapid gelation remains a significant challenge. A promising solution lies in the incorporation of trehalose, a disaccharide renowned for its ability to interact with water and proteins, forming carbohydrate vitreous structures through hydrogen bonding [17]. Trehalose exhibits low diffusion coefficients and limited molecular motions, making it an excellent candidate for imparting protective attributes against osmotic stress, heat, and cold [18]. Despite its potential benefits in improving resistance to desiccation, the use of trehalose in hydrogel formulations has been limited, warranting further investigation.

Hydrogels' self-healing mechanisms rely on reversible cross-linked structures involving dynamic covalent bonds [19,20], Diels-Alder reactions [21], disulfide bonds [22], and dynamic non-covalent interactions such as hydrogen bonding [23], ionic interactions [24] (metal coordination), host-guest interactions [25], and hydrophobic interactions [26]. The stability, self-healing capability, and mechanical properties of hydrogels are contingent on the quantity and strength of chemical bonds in their synthesized networks. However, simultaneously achieving these desirable properties in hydrogels poses a significant challenge. While stronger cross-linking structures contribute to enhanced stability and mechanical properties, these chemical bonds are irreversible upon damage, hindering the free movement and rearrangement of hydrogel chain segments necessary for the repair of broken areas [27]. Conversely, reversible cross-linking structures allow molecular chains to recombine or reorganize after damage, but they are susceptible to external conditions (e.g., temperature, pH), potentially deforming the hydrogel or reducing its original strength over time [28]. Thus, tailoring hydrogels to exhibit shape-stability and self-healing remains a formidable task.

In this study, we propose an approach to introduce trehalose into poly (vinyl alcohol)/poly (acrylic acid) (PVA/PAA) hydrogels to enhance water retention. Trehalose forms hydrogen bonds with the polymer network and attracts water molecules, thereby reducing evaporation. PVA and PAA establish intermolecular hydrogen bonds between hydroxyl and carboxyl groups. This balance between cross-linking density and self-healing properties results in a PVA/PAA hydrogel that maintains shape-stability and exhibits self-healing behavior. The novelty of this method lies in the development of a thyroid hydrogel model with high water retention and self-healing properties, offering a cost-effective and practical simulation tool for FNAB training. This model is expected to enhance the operating skills of medical personnel and promote the quality of diagnosis and treatment of thyroid lesions.

2. Materials and methods

2.1. Materials

Polyvinyl alcohol (PVA, 98–99 % Alcoholysis, Aladdin), acrylic acid (AA, >99 % (GC), MACKLIN), ammonium persulfate (APS, >98 %, Aladdin), N, N′-methylene-bis-acrylamide (MBAA, 99 %, Aladdin), D-(+)-trehalose dihydrate (99 %, Adamas-beta), rhodamine B (high purity, ≥95 % (HPLC)), and calcium carbonate (AR, 99 %, MACKLIN) were procured from commercial vendors.

2.2. Fabrication of hydrogel thyroid model

A three-dimensional (3D) thyroid geometry was digitally rendered using computer-aided design (CAD) software (UG Magics) and 3D printed to create a silicone mold. A 10 wt% polyvinyl alcohol (PVA) solution was prepared by dissolving 30 g of PVA powder in 270 mL of deionized water via magnetic stirring at 90 °C for 2 h, followed by cooling to room temperature. To synthesize the hydrogel precursor solution, 1 g of trehalose, 6.7 mg of N, N′-methylene-bis-acrylamide, and 30 mg of ammonium persulfate solution were added to 3 mL of deionized water (Solution A). Solution A was sonicated until complete dissolution occurred, after which 14 g of the 10 wt% PVA solution, 3 mL of acrylic acid, and a small amount of rhodamine B solution were incorporated. The resulting mixture was stirred thoroughly to ensure homogeneity and eliminate air bubbles. The hydrogel precursor was then injected into the silicone mold using a 10 mL syringe, sealed, and thermally cured at 80 °C for 15 min to facilitate gelation. Subsequently, the hydrogel phantom was cooled to room temperature for demolding.

2.3. Characterization of mechanical properties

Ethical considerations often necessitate the use of animal-derived tissues and organs as proxies for human analogs. In this regard, the porcine thyroid gland serves as an appropriate model due to its mechanical similarities to the human thyroid. Porcine thyroid specimens were procured from adult swine at local slaughterhouses immediately following slaughter. The extracted larynges containing the thyroid glands were promptly refrigerated at 4 °C and periodically misted with saline solution to maintain viability during transportation. The entire process, from tissue harvesting to experimental testing, was completed within 12 h post-mortem. Anatomically, the porcine thyroid is situated anterior to the second through fourth tracheal cartilaginous rings at the laryngotracheal junction, mirroring the human thyroid position.

The mechanical characterization of all samples was conducted using an Instron Model 5576 universal testing machine (Instron, USA) equipped with a 500 N load cell. Tensile and compressive tests were performed at crosshead speeds of 30 mm/min and 5 mm/min, respectively. The compressive modulus of the hydrogel specimens was quantified as the slope of the stress-strain curve within the linear region from

0 to 15 % strain. The toughness (Γ, MJ/m^{-3}) was calculated according to the following equation:

$$\Gamma = \int_{\varepsilon=0}^{\varepsilon=\varepsilon_b} \sigma_b d_\varepsilon$$

Where ε_b and σ_b are the strain and stress at hydrogel fracture, respectively.

Recovery efficiency of compression was calculated by:

$$\eta\ (\%) = (H_n / H_0) \times 100\%$$

Where H_0 is the original hydrogel height before compression, and H_n is the recovered height after the nth compressive cycle.

The recipes for the different materials are in Supplementary Materials Table S2 and Table S3.

2.4. Characterization of rheology and self-healing

The rheological properties were evaluated using an advanced rheometer (MCR302, Anton Paar). Dynamic frequency sweep experiments were performed at 25 °C with a strain amplitude of 0.1 % over an angular frequency range of 0.1–100 rad/s. The frictional behavior was probed via rotational rheometry under a constant normal force of 7 N at 25 °C and a shear rate d(gamma)/dt of 0.1 s^{-1}. The friction coefficient (μ) was calculated according to the equation:

$$\mu = 4T/3RF_N,$$

Where T is the measured torque, R is the plate radius (12.5 mm), and F_N is the normal stress.

The nonlinear viscoelastic response was interrogated through dynamic strain sweep tests conducted at 25 °C, an angular frequency of 6.283 rad/s, and strain amplitudes ranging from 0.1 % to 1000 %. Additionally, alternating step strain experiments were performed at 25 °C and 6.283 rad/s, cyclically varying the strain between 0.1 % and 400 % at 10-s intervals.

2.5. Characterization of water retention and dimensional shrinkage properties

Hydrogel specimens were exposed to ambient conditions (19–21 °C, 35–41 % relative humidity) to quantify water retention and dimensional shrinkage over time. The water retention was calculated as:

$$\text{Water retention } (\%) = (m_n/m_0) \times 100\%$$

Where m_n is the sample mass after n hours, and m_0 is the initial mass.

The dimensional shrinkage was quantified by the shrinkage ratio:

$$\text{Shrinkage ratio} = S_n/S_0$$

Where S_n is the cross-sectional area of the sample after n hours, and S_0 is the initial cross-sectional area.

2.6. Characterization of puncture performance

Puncture tests were conducted to simulate FNAB procedures using an Instron Model 5576 universal testing machine. A straight needle with a diameter of 0.57 mm was clamped at the upper end, while a compression disk was affixed to the lower end. The hydrogel samples were punctured at a crosshead speed of 480 mm/min, with the force and displacement data continuously recorded.

2.7. Characterization of structural and morphological properties

Attenuated Total Reflection-Fourier Transform Infrared Spectroscopy (FT-IR NEXUS B70) was employed to identify the functional groups present in the hydrogel networks. Freeze-dried porcine thyroid tissue and hydrogel specimens were sputter-coated with gold and examined using scanning electron microscopy (SEM VEGA3) to visualize their microstructural morphologies.

2.8. Ultrasound-guided surgery training

The hydrogel thyroid phantom was utilized for ultrasound-guided FNAB training using a PureWave PHILIPS EPIQ 5 shear wave elastography system. An ultrasound coupling agent was applied to the phantom's surface to facilitate acoustic transmission. The ultrasound probe was then used to detect and target simulated thyroid nodules within the hydrogel model.

3. Results and discussion

3.1. System design

The study was designed as a double-network (DN) hydrogel composed of interpenetrating polyvinyl alcohol (PVA) and polyacrylic acid (PAA) networks [12]. The hydrogel precursor solution with a DN architecture was formulated by dissolving the moisturizing agent trehalose, initiator ammonium persulfate (APS), crosslinker N, N′-methylene bisacrylamide (MBAA), and acrylic acid monomer in deionized water, followed by the addition of a 10 wt% PVA solution (Fig. 1A). DN hydrogels are formed through the integration of chemically and physically crosslinked polymer networks [29]. The prepared precursor solution underwent thermal initiation at 80 °C to facilitate APS-mediated free radical polymerization, resulting in the formation of a covalently crosslinked PAA network. Subsequently, the hydrogel was frozen at −20 °C to induce the formation of hydrogen bonds, thereby yielding a DN hydrogel structure. Due to the presence of abundant hydroxyl and carboxyl functional groups along the PVA and PAA chains, respectively, these moieties can participate in intermolecular hydrogen bonding interactions, conferring self-healing capabilities to the hydrogel based on the reversible nature of these physical crosslinks [30,31] (Fig. 1B). As a result, the DN hydrogel architecture not only imparts self-healing properties but also endows the material with superior mechanical characteristics and conformability. By employing indirect 3D-printing techniques, this hydrogel system can be readily fabricated into a thyroid gland phantom, enabling repeated puncture simulations for training in fine-needle aspiration biopsy procedures of the thyroid (Fig. 1C).

3.2. Structural characterization

Attenuated Total Reflection-Fourier Transform Infrared (ATR-FT-IR) spectroscopy was employed to identify the characteristic functional groups present in the hydrogel components and elucidate their molecular interactions. The FT-IR spectra of PVA, PAA, trehalose, and the PVA/PAA/trehalose hydrogel are depicted in Fig. 2A and B. The peaks at 3200-3570 cm^{-1} are attributed to the -OH stretching vibration of hydrogen bonding [32]. Compared to PVA, the -OH stretching vibration peaks in PVA/PAA/Trehalose hydrogels at 3238 cm^{-1} are gradually shifted to higher wavelengths at 3280 cm^{-1} due to the presence of PAA, which indicates that the hydrogen bonding of PVA itself is gradually being replaced by new hydrogen bonds formed between PAA and PVA. The C=O and C-O stretching vibration peaks of PAA are located at 1694 cm^{-1} and 1230 cm^{-1} [33]. In contrast, the C=O stretching vibration peak in the PVA/PAA/Trehalose hydrogel shifted to 1703 cm^{-1} and the C-O stretching vibration peak shifted to 1238 cm^{-1} at higher wavelengths, indicating that the hydrogen bond between PVA and PAA replaced the hydrogen bond of PAA itself. All these differences indicate the formation of new intermolecular hydrogen bonds between PVA and PAA. Obviously, competitive hydrogen bonding occurred in the PVA/PAA/Trehalose hydrogel material, and the hydrogen bond formed in

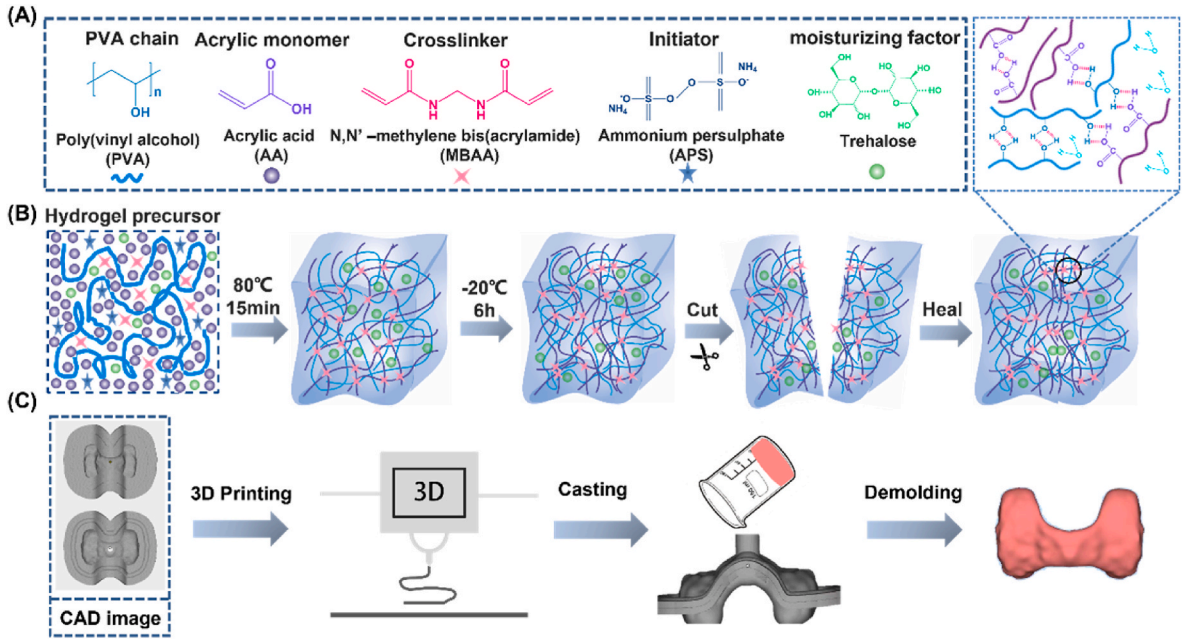

Fig. 1. Schematic representation of DN hydrogels with high water retention and self-healing properties for fabrication of thyroid models. (A) Chemical structures of the polymer chains, monomers, cross-linkers, initiators, and moisturizing factors that make up the hydrogels. (B) Schematic of the gelation process and self-healing of the hydrogel. (C) The process of modeling the thyroid gland.

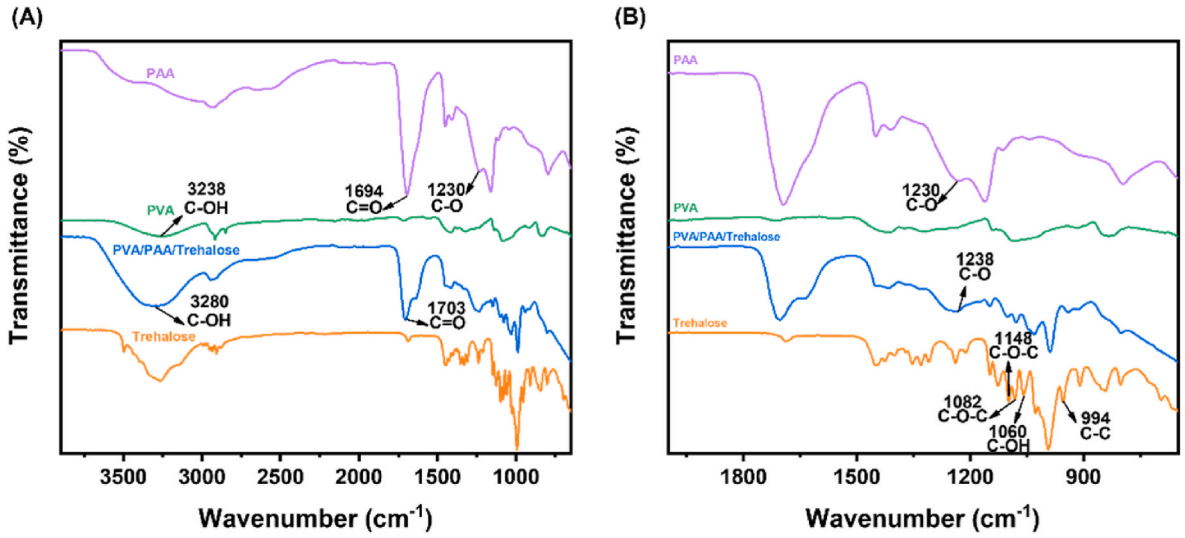

Fig. 2. FT-IR spectra of PAA, PVA, Trehalose, and PVA/PAA/Trehalose hydrogels. (A) FT-IR spectrograms of PAA, PVA, Trehalose, and PVA/PAA/Trehalose hydrogels in the 4000–650 cm^{-1} band. (B) FT-IR spectra of PAA, PVA, Trehalose, and PVA/PAA/Trehalose hydrogels in the 2000–650 cm^{-1} band.

PAA's own -COOH was gradually disengaged, and the disengaged C=O caused PVA's hydrogen bond to break replacing the hydroxyl group of PVA to form a new intermolecular hydrogen bond, which shifted the -OH peak to a higher wave number [32]. The C-C stretching vibration peak of the trehalose molecule was located at 994 cm^{-1}, and the characteristic peaks at 1082 cm^{-1} and 1148 cm^{-1} corresponded to the asymmetric stretching vibration of the C-O-C bridging band and non-bridging modes on the trehalose molecule, and the peak located at 1060 cm^{-1} was attributed to the bending vibration of the C-OH of the trehalose molecule [34]. PVA/PAA/Trehalose The broadening of the C-OH bending vibration peak of the trehalose molecule in the hydrogel may be attributed to the formation of intermolecular hydrogen bonds between the trehalose and the polymer chains.

3.3. *Mechanical properties and shape fidelity*

The mechanical properties of DN hydrogels varied with composition, and Fig. S1 shows the gelation of different concentrations of acrylic acid (AA). Specifically, the compressive modulus and toughness of DN hydrogels increase accordingly with the increase of monomer AA content, ranging from 1.9 KPa to 17.3 KPa and from 0.012 MJ m^{-3} to 0.0682 MJ m^{-3}, respectively, which may be attributed to the fact that the introduction of PAA increases the intersections and entanglements of the polymer chains in the network and increases the cross-link density of the network, making the molecular chains more difficult to move under force, thus increasing the compressive and toughness of the hydrogel. Meanwhile, at a certain concentration of cross-linker, the DN hydrogels all exhibited excellent tensile properties, with strains at break exceeding

400 % (Fig. 3A–C). The effects of different cross-linker contents on the mechanical properties of DN hydrogels are investigated in Fig. 3D–F. It can be seen that as the MBAA content increases from 0.1 % to 0.25 % (compared to monomer), the compression modulus of DN hydrogels increases, the toughness decreases, and the hydrogels become stiffer and more brittle, which can be attributed to an increase in the chemically cross-linking "rigid" network. The higher crosslink density results in a more compact network structure. Fig. S2A and B show images of the porcine thyroid gland. Notably, the tensile stress-strain curves of porcine thyroid tissues did not have obvious breaking points, which may be due to the inhomogeneity of the porcine thyroid tissue-like (Fig. S3A). (Figs. S3B–C) show the compressive properties of porcine thyroid tissues, in which the compressive modulus ranged from 2.9 KPa to 4.7 KPa, which was very soft. From the above summary of mechanical properties, it can be obtained that DN hydrogel can effectively mimic the biomechanical properties of porcine thyroid tissue. The DN hydrogel formulation with 15 wt% acrylic acid and 1:1000 MBAA: AA molar ratio, yielding a compressive modulus of 4.8 kPa, was selected for further study due to its close biomimicry of porcine thyroid tissue softness.

Excellent shape-fidelity is essential for producing effective simulation models, as inevitable distortions from handling and storage can render soft tissue-mimicking hydrogels unusable in practical medical training applications [35]. The DN hydrogel structure endowed the materials with remarkable flexibility, withstanding severe knotting, stretching to more than seven times its initial length (Fig. 4A–C), and large compressive deformations without collapse or rupture (Fig. 4D–F). Upon load removal, the cylindrical hydrogels could fully recover their original dimensions, exhibiting exceptional shape retention capabilities. Comparative compression testing at 80 % strain and 30 mm/min revealed superior shape recovery for the DN hydrogels relative to their single network PVA and PAA counterparts (Fig. S4). After 10 cycles, the PVA hydrogel exhibited only 82.54 % recovery, whereas the DN and PAA hydrogels maintained 98.46 % and 94.82 % recovery, respectively, owing to the chemically cross-linked network structure. Notably, the PVA hydrogel fractured after 10 cycles, while the DN hydrogel retained 95.8 % recovery even after 30 compression cycles, outperforming the 90.79 % recovery of the PAA hydrogel. This demonstrates the DN hydrogels' resistance to significant plastic deformation or strength degradation under extreme compressive strains, enabling rapid shape recovery facilitated by the synergistic chemical and physical cross-linking within the DN architecture (Figs. S5A–D), show the compression cycles of different hydrogels.

3.4. Rheological and self-healing properties

To elucidate the viscoelastic, self-healing, and lubricious characteristics, rheological measurements were conducted on the thyroid tissue-mimicking DN hydrogels (Fig. 5A). Dynamic frequency sweep experiments confirmed the viscoelastic nature, with the storage modulus (G′) exceeding the loss modulus (G′′) across the entire frequency range under low strain amplitudes, signifying solid-like elastic behavior (Fig. 5B). The tanδ values of hydrogels simulating thyroid tissues ranged from 0.368 to 0.538, indicating that hydrogels have flow properties close to those of soft tissues (Fig. 5C) [13]. To further characterize the tactile properties of the hydrogel, its friction coefficient was tested. Fig. S6 shows the friction coefficient of the porcine thyroid gland, which increased from 0.03 to 0.3 for the porcine thyroid tissue as the shear time increased. It should be noted that the friction coefficient of the hydrogel decreased from 0.289 to 0.049 before 140 s, which is because the normal phase force loaded between 140 s had not yet reached 7 N, The friction coefficients of the hydrogels ranged from 0.047 to 0.170 after 140 s (Fig. 5D). This may be because, with the increase in shear time, the molecular chains within the hydrogels may interact, causing the cross-linking points to interlock, thus increasing the friction between the molecular chains. in the actual process, the thyroid tissue will not be continuously rubbed for a long time, so only the wet slipperiness of the hydrogel is close to the initial value of the thyroid tissue. The hydrogel still shows excellent wet slipperiness under prolonged shear. Based on the comprehensive mechanical properties, it can be concluded that the hydrogel has a tactile sensation similar to that of the porcine thyroid gland (Fig. 5E). shows the strain scan results of the hydrogel, where the intersection of the energy storage modulus G′ and loss modulus G′′ is 210 %, indicating that at this point the hydrogel structure breaks down, i.e., is cleaved from each other. To demonstrate the self-healing behavior of the hydrogels, they were tested with alternating-step strain scans (Fig. 5F). shows the recovery of the hydrogel network at low strains and

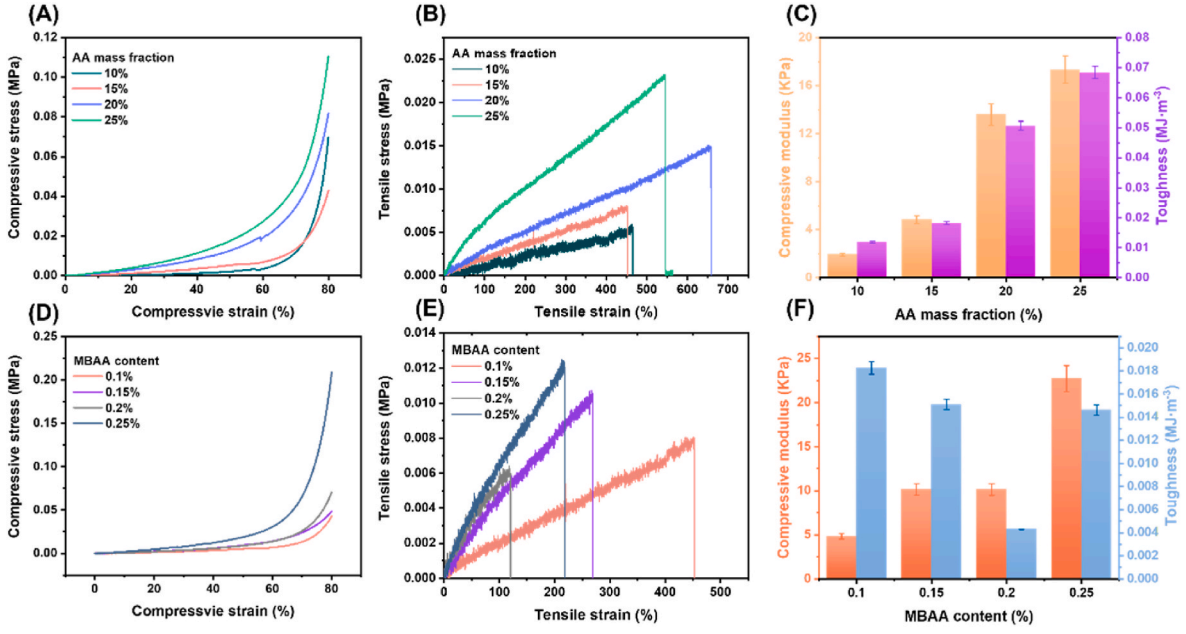

Fig. 3. Mechanical properties of hydrogels. (A) Compressive stress-strain curves with different AA mass fractions. (B) Tensile stress-strain curves with different AA mass fractions. (C) Corresponding compressive modulus and toughness with different mass AA fractions. (D) Compressive stress-strain curves with different MBAA content. (E) Tensile stress-strain curves with different MBAA content. (F) Corresponding compressive modulus and toughness with different MBAA content.

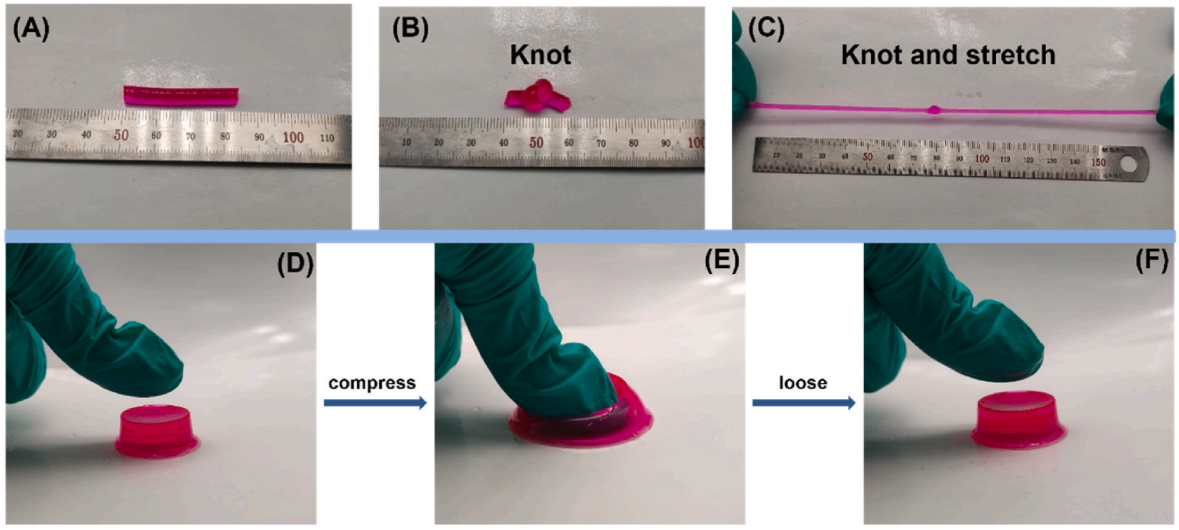

Fig. 4. Hydrogel subjected to kinking and shape recovery. (A–C) Hydrogel undergoing kinking and large stretching. (D–F) Hydrogel undergoing compression and recovery.

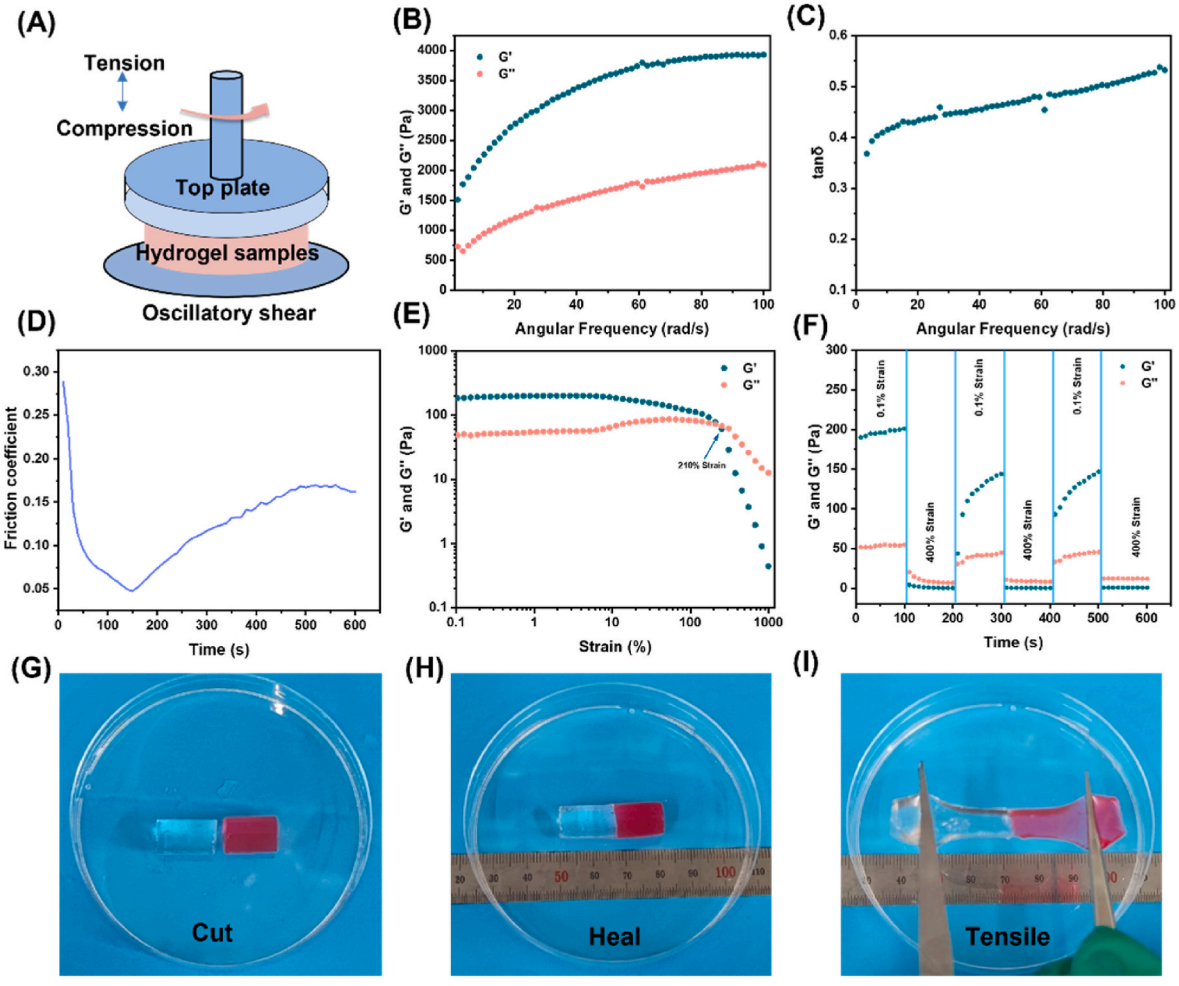

Fig. 5. Pictures of rheological properties and macroscopic self-healing behavior of hydrogels. (A) Schematic of the rheological measurements of the hydrogel. (B–C) Oscillation frequency scans and viscoelasticity (tan δ, G"/G′) of hydrogels. (D) Friction coefficient of the hydrogel. (E) G′ and G" of DN hydrogel in strain scan test. (F) Rheological properties of hydrogel when switching from 0. 1 %–400 % in an alternating step strain scan test. (G) Cutting of hydrogel, (H) self-healing of two halves, (I) stretching after self-healing.

the destruction of the hydrogel network at high strains. Specifically, at high dynamic strain (400 %), the hydrogel's G′ decreased from 130.13 KPa to 1.21 KPa, and G'' decreased from 39.59 KPa to 8.00 KPa and increased to 39.59 KPa, where G'' > G′, indicating the disruption of the hydrogel structure. However, at low dynamic strain (0.1 %), G′ was able to recover to its initial original level, indicating that the hydrogel network can be effectively restored. This reproducible self-healing behavior is attributed to reversible physical cross-linking in the network. To see the self-healing changes more clearly, the cylindrical hydrogel was cut into two halves; one half was stained with rhodamine B, and then the two halves were touched together without external force. Although rhodamine may affect the mechanical properties of the hydrogel [29], the minimal amount used in this study ensures a negligible impact. The samples were self-healed at ambient temperature for 24 h. It was found that the samples were able to withstand stretching (>300 %) and showed good self-healing properties (Fig. 5G–I). We also performed self-healing tensile experiments on the hydrogels (Figs. S7A–B), and the self-healing hydrogels were able to return about 23 % of their initial strength at smaller contact surfaces.

3.5. Water retention properties

High water retention is crucial for enhancing the simulation fidelity, maneuverability, and useable duration of hydrogel models, particularly for thyroid fine-needle aspiration training sessions lasting approximately 6 h. Therefore, this work focused on the water retention effect of hydrogel for 6 h. Early studies have shown that glycerol reduces the vapor pressure of hydrogels by hydrogen bonding to water molecules, thus reducing water evaporation [15]. In this work, trehalose, which can form hydrogen bonding interactions with water molecules, was used. As a natural moisturizing factor, trehalose has multiple hydroxyl functional groups that can form hydrogen bonding interactions with water molecules, enabling trehalose to adsorb and maintain the stability of water molecules in the hydrogel, and the hydroxyl groups on its sugar ring can also be bonded to the polymer chain through hydrogen bonding, thus enhancing the water retention properties of the hydrogel. Fig. 6A shows that after 6h at ambient temperature, 15 wt% PVA became significantly smaller in size and contracted extremely fast, while PVA/PAA hydrogels and hydrogels soaked in glycerol solution also showed significant size reduction. Interestingly, the size of the hydrogel with a small amount of trehalose added was very close to the initial size after 6h. Meanwhile, introducing trehalose can effectively reduce the drying behavior of hydrogels. Fig. 6B shows that the water retention of ordinary PVA hydrogel at ambient temperature for 6h was only 84 %, while PVA/PAA hydrogel with a DN structure was able to increase the water retention to 88.9 %, which may be attributed to the fact that the DN structure has a larger pore structure and surface area, which enables it to absorb more water molecules. Although soaking in a highly concentrated glycerol solution increases the water retention of the hydrogel to 95.5 %, prolonged soaking causes the hydrogel to form wrinkles. In comparison, the addition of a small amount of trehalose increased the hydrogel's water retention to 91.2 %. When 20 wt% trehalose was incorporated, the water retention further improved to 94.7 %. Although this is slightly lower than the retention achieved by immersion in a high-concentration glycerol solution, the incorporation of trehalose had minimal impact on the hydrogel's original shape. This indicates that trehalose-modified hydrogels exhibit excellent adaptability for the fabrication of thyroid models used in FNAB training. (Specific water retention in Supplementary Material Table S1). Furthermore, dimensional shrinkage tests revealed that after 6 h, the hydrogel immersed in glycerol solution exhibited a maximum shrinkage ratio of only 0.89, while the trehalose-modified hydrogel reached 0.96—significantly higher than the hydrogel without trehalose—indicating superior anti-shrinkage performance (Fig. 6C). These results confirm that trehalose-modified PVA/PAA hydrogels can effectively slow dehydration through strong hydrogen bonding interactions. Fig. 6D shows the compression modulus of the trehalose-modified PVA/PAA hydrogel at both the initial time and after 6 h. It should be noted that the original hydrogel has a compression

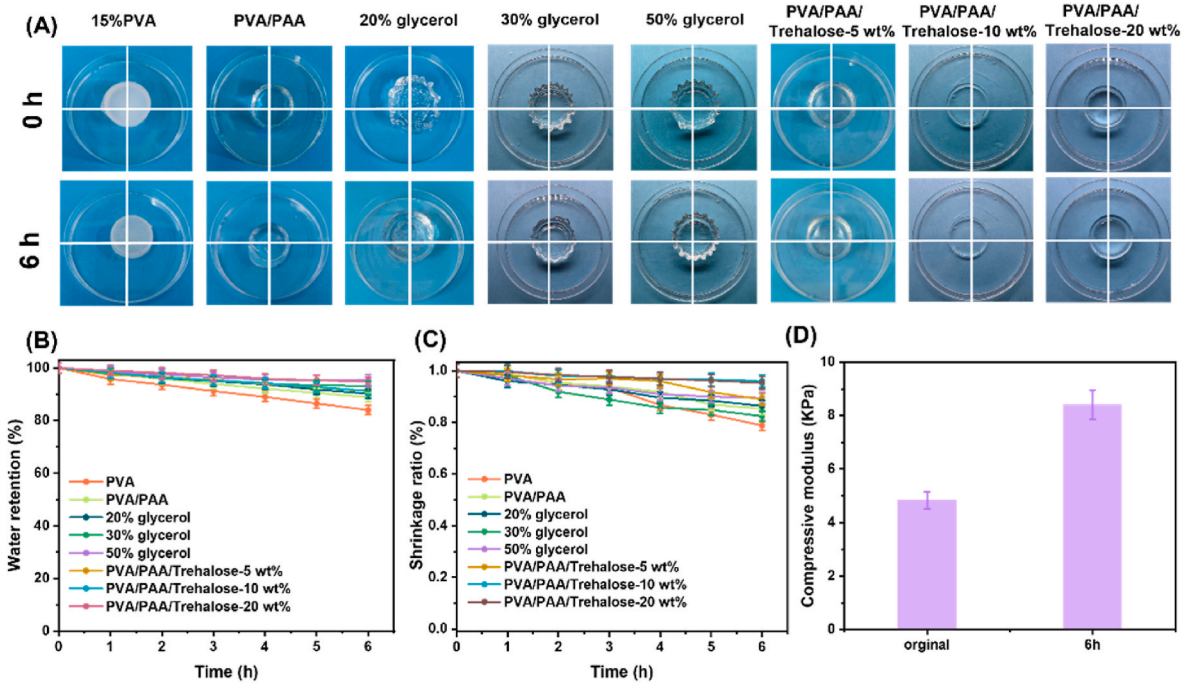

Fig. 6. Water retention properties of hydrogels. (A) Drying behavior of PVA, PVA/PAA, and hydrogels soaked in 20 %, 30 %, and 50 % glycerol solution, as well as trehalose (−5 wt%, −10 wt%, −20 wt %) modified hydrogels at 0h and 6h. (B) Water retention of PVA, PVA/PAA, and hydrogels soaked in 20 %, 30 %, and 50 % glycerol solution, and trehalose (−5 wt%, −10 wt%, −20 wt %) modified hydrogel over 0–6h. (C) shrinkage ratio of PVA, PVA/PAA, and hydrogels soaked in 20 %, 30 %, and 50 % glycerol solution, and trehalose (−5 wt%, −10 wt%, −20 wt %) modified hydrogel over 0–6h. (D) Comparison of compression modulus of trehalose hydrogels at initial and 6h.

modulus of 4.8 KPa, which is very small and exhibits a softness like that of soft tissues. The compression modulus at 6 h is 8.4 KPa, which is higher than that of the initial compression modulus, but since the compression modulus is already very small, in terms of its true softness, it is almost indistinguishable from the softness of the initial hydrogel. These results highlight the efficacy of trehalose-modified dual network PVA/PAA hydrogels in retarding dehydration through strong hydrogen bonding interactions, enabling their use as thyroid phantom models for fine-needle aspiration training.

3.6. Puncture performance

To evaluate the puncture force magnitudes relevant to simulating thyroid FNAB procedures, puncture testing was performed on the hydrogel samples. This technique has previously been used to validate skin simulation materials by replicating needle injection force profiles in additive manufacturing medical models [36]. Compression testing was performed on an Instron Model 5576 universal materials testing machine equipped with a 500 N transducer (Fig. 7A). The steel needle used to puncture the hydrogel sample is clamped with a fixture at the upper end, and a compression disk is attached at the lower end. The test tube holder is placed on the compression disk, and due to the hole structure of the holder itself, the hydrogel sample can be placed in the middle of the holes of the holder, and then the penetration force during the puncture is tested using the compression procedure. The needles used for thyroid fine-needle aspiration procedures are usually 23- or 25-gauge needles with diameters of 0.573 mm and 0.510 mm, respectively, and a puncture speed of 8 mm/s [37,38]. Therefore, to accurately test the puncture force of the simulated hydrogel and to simulate the fine needle puncture process of the thyroid gland, a steel needle with a diameter of 0.57 mm and a compression speed of 480 mm/min was selected to puncture the hydrogel sample and record the relationship between the force and displacement, and a photograph of the puncture site is shown in Fig. 7B. In the test results, the steel needle starts to penetrate the hydrogel surface at a displacement of 25 mm, and the penetration force gradually increases with the deepening of the penetration depth, which may be because the hydrogel sample will be locally deformed in the penetration area to form a more solid structure, which increases the difficulty and resistance of the needle to penetrate. When the penetration force reaches its maximum, a sharp decrease occurs, resulting in an obvious mutation point, called the penetration point, indicating that the steel needle has already penetrated the bottom layer of the hydrogel sample, and the penetration force obtained from the test was 0.98 N (Fig. 7C). When the steel needle penetrated the bottom layer (rupture stage), the puncture force of the hydrogel sample fell within the range of 0.52–0.71 N, which is close to the range of force magnitude required by a suture needle to puncture human tissues during the suturing process [39]. Therefore, the use of PVA/PAA/Trehalose hydrogel for other simulation models, such as the skin used for sutures, is also instructive. Notably, the measured puncture forces fell within the reported range of 0.87–1 N for needle insertion into tumor-free thyroid tissue [39], substantiating the suitability of the PVA/PAA/trehalose hydrogels as reliable thyroid gland phantoms for FNAB training simulations.

3.7. Microscopic surface morphology

To demonstrate the similarity between PVA/PAA/Trehalose hydrogel and porcine thyroid microstructure, the microstructural morphologies of the PVA/PAA/trehalose hydrogels and porcine thyroid tissue were characterized using SEM at 1000x magnification. The porcine thyroid exhibited a locally porous architecture with an average pore size of approximately 4.4 μm (Fig. 8A). Additionally, the extreme inhomogeneity observed in the porcine thyroid tissue microstructure (Fig. 8B) accounts for the absence of distinct fracture points during tensile deformation. In contrast, the PVA/PAA/trehalose hydrogel showed a uniformly porous microstructure (Fig. 8C–D), with an average pore size comparable to that of porcine thyroid tissue, approximately 4.8 μm. Figs. S8A–B show the pore size distribution on SEM images of porcine thyroid and PVA/PAA/Trehalose hydrogels, respectively. This corroborates that the biomimetic hydrogel organ models accurately recapitulate the porous microarchitecture and mechanical compliance of the native thyroid gland. Furthermore, the uniform pore morphology of the hydrogels contributes to their outstanding tensile properties.

3.8. Ultrasound-guided surgery training

The fabricated 3D thyroid hydrogel model was employed for ultrasound-guided FNAB procedure training. Fig. S9A shows a hydrogel thyroid model with dimensions corresponding to a 1:1 scale of a human thyroid organ, featuring lesion simulants placed on its surface (Fig. S6B). Figures S9C-D illustrate the training venue for ultrasound-guided thyroid FNAB procedures and the trainer's field operations. An ultrasound probe was placed on the thyroid module to locate and identify the thyroid nodule, with subsequent adjustment of the ultrasound instrument parameters to obtain a clear image. Fig. 9A shows the ultrasound image of the fabricated thyroid model, wherein the bright white spot on the left represents the simulated thyroid nodule. Fig. 9B demonstrates a trainer undergoing ultrasound-guided thyroid FNAB procedure training, with a successful puncture evidenced by the penetration of the puncture needle into the nodule simulator, as visualized on the ultrasound

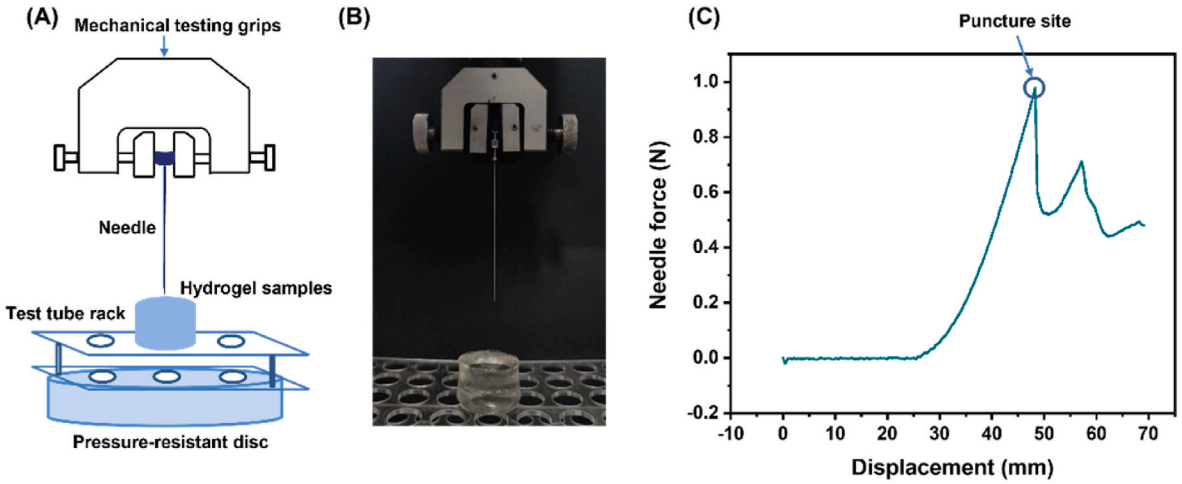

Fig. 7. Puncture testing of hydrogels. (A) Puncture schematic diagram. (B) Field diagram of puncture. (C) Force-displacement curve of hydrogel puncture.

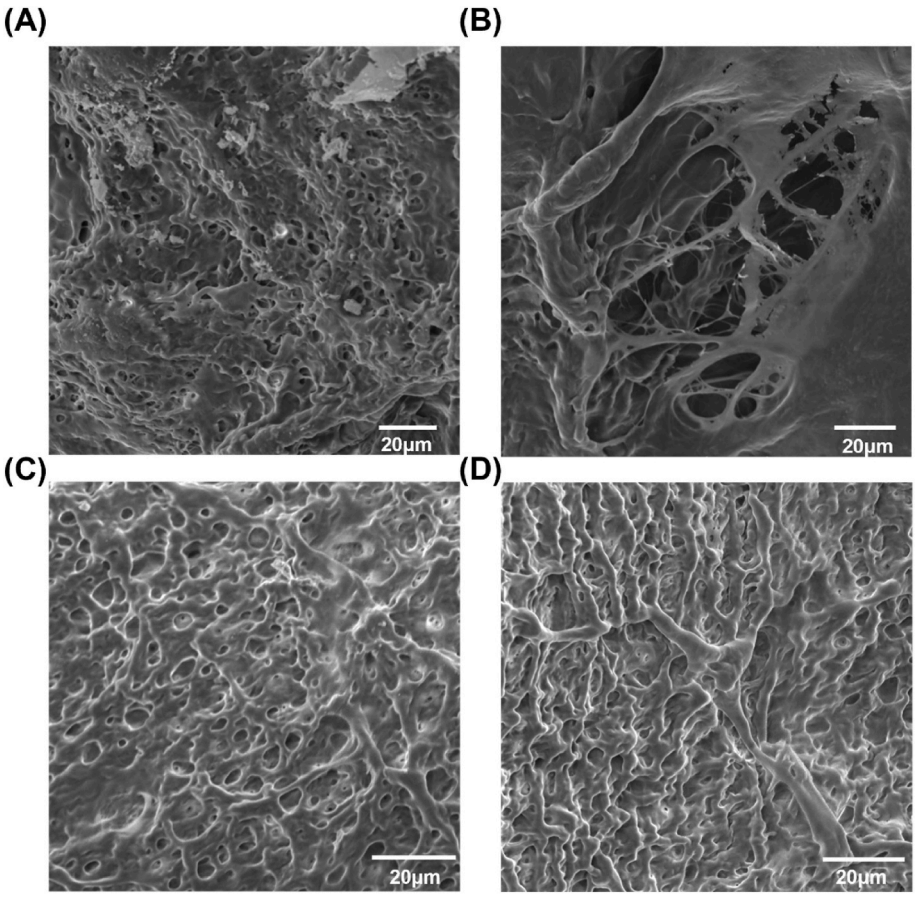

Fig. 8. SEM images of porcine thyroid and PVA/PAA/Trehalose hydrogel. (A–B) SEM image of the porcine thyroid gland. (C–D) SEM image of PVA/PAA/Trehalose hydrogel.

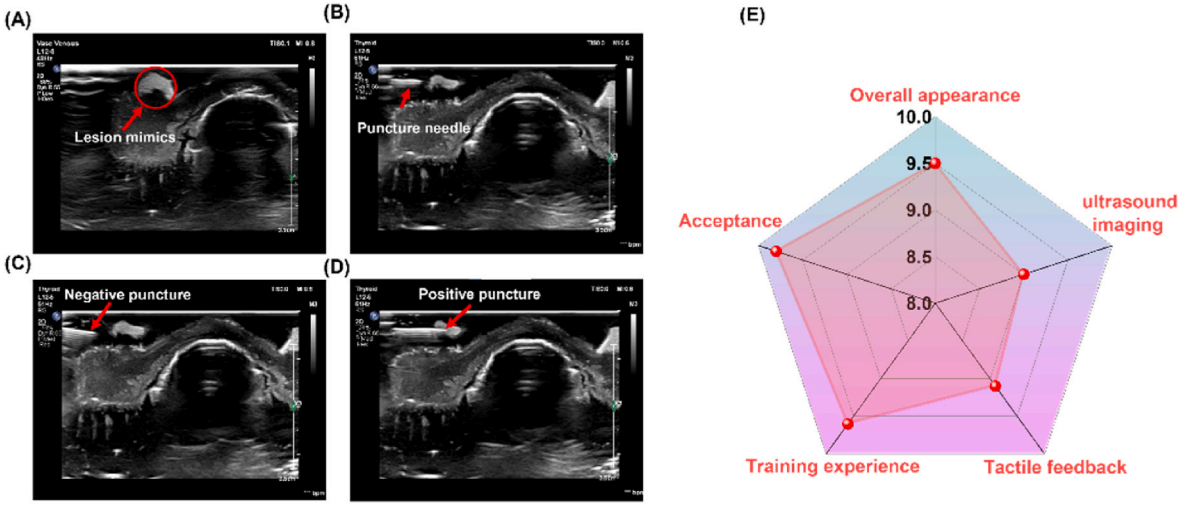

Fig. 9. Ultrasound-guided training for fine needle aspiration of the thyroid. (A) Images of the thyroid model under ultrasound. (B) Performing the puncture operation. (C) Failed puncture training. (D) Successful puncture training. (E) Ultrasound specialists rated five dimensions (overall appearance, ultrasound image, tactile feedback, training experience, and acceptance).

imager. Upon determining the nodule's location, the trainer utilized the puncture needle to penetrate the hydrogel thyroid module and gradually approach the nodule. Given the limited experience, the novice surgeon did not accurately puncture the lesion simulants on the initial puncture maneuver, as evidenced by the ultrasound image depicting the needle puncturing the bottom and edges of lesion simulants (Fig. 9C and Videos S1, S2, S5, and S9). However, this did not pose a significant concern, as the thyroid model facilitated repeated puncture maneuvers, allowing the novice physician the opportunity for trial and error. After regaining confidence following the initial puncture failure, the novice surgeon, leveraging the experience gained during the previous puncture operations, was able to accurately control the puncture force, speed, and

needle compression, successfully puncturing the target and completing the simulated ultrasound-guided FNA of the thyroid gland (Fig. 9D and Videos S3, S4 and S6). Of course, there were a few novice physicians who were able to puncture the lesion simulant on the first try (Videos S7, S8, and S10). To further assess the effectiveness of the simulation product, five novice surgeons evaluated the training content on a five-point scale from 0 (very poor) to 5 (very good), awarding a rating of 4.6 ± 0.1, indicating an "excellent" assessment for ultrasound-guided training in thyroid gland FNAB. Ultrasound specialists rated 9.5, 9.0, 9.1, 9.6, and 9.8 out of 10 on the five dimensions of overall appearance, ultrasound image, tactile feedback, training experience, and acceptance (Fig. 9E). Thus, the training results suggest that the hydrogel thyroid model can serve as an excellent training platform, providing a realistic clinical environment for surgical training.

Supplementary data related to this article can be found online at doi:

4. Conclusions

In conclusion, we present a highly water-retentive and self-healing hydrogel thyroid model fabricated using inexpensive and commercially available materials. However, excessive amounts of trehalose can affect the gelation time of the hydrogel, making it necessary to select an appropriate amount based on the hydrogel formulation. The synergistic combination of these properties grants the model reusability and cost-effectiveness, eliminating the need for disposable models. The fabricated thyroid models exhibit mechanical properties, tactile sensations, and microscopic surface structures highly reminiscent of porcine thyroid tissue, adequately fulfilling the requirements for surgical training in clinical scenarios. Notably, ultrasound specialists gave high ratings (9.5, 9.0, 9.1, 9.6, 9.8) for overall appearance, ultrasound image, tactile feedback, training experience, and acceptance. Five novice surgeons also awarded high ratings (4.6 ± 0.1) to the hydrogel thyroid model after training. Integration of a simulation-based modeling approach into surgical training facilitated the practice of hand-eye coordination and the improvement of surgical skills among novice physicians. Therefore, these highly water-retentive and self-healing hydrogel thyroid models provide a reasonable training platform, emerging as a promising tool to enhance the safety and efficiency of operations in future clinical practice.

CRediT authorship contribution statement

Liang Ma: Writing – original draft, Visualization, Validation, Investigation, Formal analysis, Data curation, Conceptualization. **Zhihao Zhu:** Writing – review & editing, Methodology, Investigation. **Shijie Yu:** Writing – review & editing, Investigation. **Sidney Moses Amadi:** Writing – review & editing. **Fei Zhao:** Funding acquisition. **Jing Zhang:** Supervision, Resources, Project administration. **Zhifei Wang:** Writing – review & editing, Supervision, Project administration, Funding acquisition.

Declaration of competing interest

The authors declare that they have no known competing financial interests or personal relationships that could have appeared to influence the work reported in this paper.

Acknowledgments

The authors thank the Department of Ultrasound, Zhejiang Provincial People's Hospital, and Sidney Moses Amadi for language assistance in writing. This study was supported by The Special Project for Key R&D Task of the Xinjiang Uygur Autonomous Region (Project No.2023B03010-1), The Science and Technology Cooperation Project of Zhejiang Provincial Department of Science and Technology (2024C04027), and The General Research Project of Zhejiang Provincial Department of Education (Y202249352).

Appendix A. Supplementary data

Supplementary data to this article can be found online at https://doi.org/10.1016/j.mtbio.2024.101334.

Data availability

Data will be made available on request.

References

[1] A. Shapira, T. Dvir, 3D tissue and organ printing—hope and reality, Adv. Sci. 8 (2021) 2003751, https://doi.org/10.1002/advs.202003751.
[2] S. Jasim, D.S. Dean, H. Gharib, Fine-needle aspiration of the thyroid gland, in: K. R. Feingold, B. Anawalt, M.R. Blackman, A. Boyce, G. Chrousos, E. Corpas, W.W. de Herder, K. Dhatariya, K. Dungan, J. Hofland, S. Kalra, G. Kaltsas, N. Kapoor, C. Koch, P. Kopp, M. Korbonits, C.S. Kovacs, W. Kuohung, B. Laferrère, M. Levy, E. A. McGee, R. McLachlan, M. New, J. Purnell, R. Sahay, A.S. Shah, F. Singer, M. A. Sperling, C.A. Stratakis, D.L. Trence, D.P. Wilson (Eds.), Endotext, MDText.com, Inc., South Dartmouth (MA), 2000. http://www.ncbi.nlm.nih.gov/books/NBK285544/. (Accessed 19 January 2024).
[3] C.-L. Cao, Q.-L. Li, J. Tong, L.-N. Shi, W.-X. Li, Y. Xu, J. Cheng, T.-T. Du, J. Li, X.-W. Cui, Artificial intelligence in thyroid ultrasound, Front. Oncol. 13 (2023) 1060702, https://doi.org/10.3389/fonc.2023.1060702.
[4] L.-Q. Zhou, J.-Y. Wang, S.-Y. Yu, G.-G. Wu, Q. Wei, Y.-B. Deng, X.-L. Wu, X.-W. Cui, C.F. Dietrich, Artificial intelligence in medical imaging of the liver, World J. Gastroenterol. 25 (2019) 672–682, https://doi.org/10.3748/wjg.v25.i6.672.
[5] L. Ma, S. Yu, X. Xu, S. Moses Amadi, J. Zhang, Z. Wang, Application of artificial intelligence in 3D printing physical organ models, Mater, Today Bio 23 (2023) 100792, https://doi.org/10.1016/j.mtbio.2023.100792.
[6] C. Brenna, S. Das, Imperfect by design: the problematic ethics of surgical training, J. Med. Ethics 0 (2019) 1–4, https://doi.org/10.1136/medethics-2019-105837.
[7] E.R. Perica, Z. Sun, A systematic review of three-dimensional printing in liver disease, J. Digit. Imag. 31 (2018) 692–701, https://doi.org/10.1007/s10278-018-0067-x.
[8] A. Ganguli, G.J. Pagan-Diaz, L. Grant, C. Cvetkovic, M. Bramlet, J. Vozenilek, T. Kesavadas, R. Bashir, 3D printing for preoperative planning and surgical training: a review, Biomed, Microdevices 20 (2018) 65, https://doi.org/10.1007/s10544-018-0301-9.
[9] H. Yang, M. Ji, M. Yang, M. Shi, Y. Pan, Y. Zhou, H.J. Qi, Z. Suo, J. Tang, Fabricating hydrogels to mimic biological tissues of complex shapes and high fatigue resistance, Matter 4 (2021) 1935–1946, https://doi.org/10.1016/j.matt.2021.03.011.
[10] C. Liaw, S. Ji, M. Guvendiren, Human tissue models: engineering 3D hydrogels for personalized in vitro human tissue models, Adv. Healthc. Mater. 7 (2018) 1870021, https://doi.org/10.1002/adhm.201870021.
[11] C.-W. Tu, F.-C. Tsai, J.-K. Chen, H.-P. Wang, R.-H. Lee, J. Zhang, T. Chen, C.-C. Wang, C.-F. Huang, Preparations of tough and conductive PAMPS/PAA double network hydrogels containing cellulose nanofibers and polypyrroles, Polym 12 (2020) 2835, https://doi.org/10.3390/polym12122835.
[12] D. Liu, P. Jiang, Y. Wang, Y. Lu, J. Wu, X. Xu, Z. Ji, C. Sun, X. Wang, W. Liu, Engineering tridimensional hydrogel tissue and organ phantoms with tunable springiness, Adv. Funct. Mater. 33 (2023) 2214885, https://doi.org/10.1002/adfm.202214885.
[13] X. Xu, S. Yu, L. Ma, J. Mao, H. Chen, Z. Zhu, L. Wang, H. Lin, J. Zhang, Z. Wang, Multifunctional high-simulation 3D-printed hydrogel model manufacturing engineering for surgical training, Int. J. Bioprinting 9 (2023) 766, https://doi.org/10.18063/ijb.766.
[14] Z. Li, Z. Liu, T.Y. Ng, P. Sharma, The effect of water content on the elastic modulus and fracture energy of hydrogel, Extreme Mech. Lett. 35 (2020) 100617, https://doi.org/10.1016/j.eml.2019.100617.
[15] X. Sui, H. Guo, C. Cai, Q. Li, C. Wen, X. Zhang, X. Wang, J. Yang, L. Zhang, Ionic conductive hydrogels with long-lasting antifreezing, water retention and self-regeneration abilities, Chem. Eng. J. 419 (2021) 129478, https://doi.org/10.1016/j.cej.2021.129478.
[16] P. He, J. Wu, X. Pan, L. Chen, K. Liu, H. Gao, H. Wu, S. Cao, L. Huang, Y. Ni, Anti-freezing and moisturizing conductive hydrogels for strain sensing and moist-electric generation applications, J. Mater. Chem. A 8 (2020) 3109–3118, https://doi.org/10.1039/C9TA12940E.
[17] M. Burek, S. Waśkiewicz, S. Awietjan, I. Wandzik, Thermoresponsive hydrogels with covalently incorporated trehalose as protein carriers, React. Funct. Polym. 119 (2017) 105–115, https://doi.org/10.1016/j.reactfunctpolym.2017.08.009.
[18] C. Ash, Trehalose confers superpowers, Science 358 (2017) 1398.5–1399, https://doi.org/10.1126/science.358.6369.1398-e.
[19] Q. Zhang, S. Niu, L. Wang, J. Lopez, S. Chen, Y. Cai, R. Du, Y. Liu, J. Lai, L. Liu, C. Li, X. Yan, C. Liu, J.B.-H. Tok, X. Jia, Z. Bao, An elastic autonomous self-healing capacitive sensor based on a dynamic dual crosslinked chemical system, Adv. Mater. 30 (2018) 1801435, https://doi.org/10.1002/adma.201801435.
[20] Y.-L. Tsai, P. Theato, C.-F. Huang, S. Hsu, A 3D-printable, glucose-sensitive and thermoresponsive hydrogel as sacrificial materials for constructs with vascular-like

channels, Appl. Mater. Today 20 (2020) 100778, https://doi.org/10.1016/j.apmt.2020.100778.
[21] X. Li, R. Yu, Y. He, Y. Zhang, X. Yang, X. Zhao, W. Huang, Four-dimensional printing of shape memory polyurethanes with high strength and recyclability based on Diels-Alder chemistry, Polymer 200 (2020) 122532, https://doi.org/10.1016/j.polymer.2020.122532.
[22] J. Wu, X. Liu, L. Chen, J. Du, L. Ji, Y. Peng, L. Liu, Z. Xu, X. Lin, W. Lin, Y. Sun, G. Yi, Rapid self-healing and high-mechanical-strength epoxy resin coatings incorporating dynamic disulfide bonds, ACS Appl. Polym. Mater. 6 (2024), https://doi.org/10.1021/acsapm.4c00346, 4778-4778.
[23] L. Chen, J. Xu, M. Zhu, Z. Zeng, Y. Song, Y. Zhang, X. Zhang, Y. Deng, R. Xiong, C. Huang, Self-healing polymers through hydrogen-bond cross-linking: synthesis and electronic applications, Mater, Horiz 10 (2023) 4000–4032, https://doi.org/10.1039/D3MH00236E.
[24] K. Auepattana-Aumrung, D. Crespy, Self-healing and anticorrosion coatings based on responsive polymers with metal coordination bonds, Chem. Eng. J. 452 (2023) 139055, https://doi.org/10.1016/j.cej.2022.139055.
[25] W.-Y. Guo, M.-G. Ma, Conductive nanocomposite hydrogels for flexible wearable sensors, J. Mater. Chem. A (2024), 10.1039.D3TA08069B.
[26] M. Li, Z. Liu, Y. Hu, R. Li, Y. Cao, A hydrophobic eutectogel with excellent underwater Self-adhesion, Self-healing, Transparency, Stretchability, ionic Conductivity, and fully recyclability, Chem. Eng. J. 472 (2023) 145177, https://doi.org/10.1016/j.cej.2023.145177.
[27] A. Durand-Silva, K.P. Cortés-Guzmán, R.M. Johnson, S.D. Perera, S.D. Diwakara, R. A. Smaldone, Balancing self-healing and shape stability in dynamic covalent photoresins for stereolithography 3D printing, ACS Macro Lett. 10 (2021) 486–491, https://doi.org/10.1021/acsmacrolett.1c00121.
[28] J. Yang, Y. Chen, L. Zhao, J. Zhang, H. Luo, Constructions and properties of physically cross-linked hydrogels based on natural polymers, Polym. Rev. 63 (2023) 574–612, https://doi.org/10.1080/15583724.2022.2137525.
[29] C.-H. Wu, C.-W. Tu, J. Aimi, J. Zhang, T. Chen, C.-C. Wang, F. Huang, Mechanochromic double network hydrogels as a compression stress sensor, Polym. Chem. 11 (2020) 6423–6428, https://doi.org/10.1039/D0PY01075H.
[30] T. Liu, C. Jiao, X. Peng, Y.-N. Chen, Y. Chen, C. He, R. Liu, H. Wang, Super-strong and tough poly(vinyl alcohol)/poly(acrylic acid) hydrogels reinforced by hydrogen bonding, J. Mater. Chem. B 6 (2018) 8105–8114, https://doi.org/10.1039/C8TB02556H.
[31] L. Guadagno, L. Vertuccio, C. Naddeo, E. Calabrese, G. Barra, M. Raimondo, A. Sorrentino, W.H. Binder, P. Michael, S. Rana, Self-healing epoxy nanocomposites via reversible hydrogen bonding, Compos. Part B Eng. 157 (2019) 1–13, https://doi.org/10.1016/j.compositesb.2018.08.082.
[32] N. Chen, J. Zhang, The role of hydrogen-bonding interaction in poly(vinyl alcohol)/poly(acrylic acid) blending solutions and their films, Chin. J. Polym. Sci. 28 (2010) 903–911, https://doi.org/10.1007/s10118-010-9167-x.
[33] I. Manavi-Tehrani, M. Rabiee, M. Parviz, M.R. Tahriri, Z. Fahimi, Preparation, characterization and controlled release investigation of biocompatible pH-sensitive PVA/PAA hydrogels, Macromol. Symp. 296 (2010) 457–465, https://doi.org/10.1002/masy.201051062.
[34] D. Liu, P. Jiang, Y. Hu, Y. Lu, Y. Wang, J. Wu, D. Hu, T. Wu, X. Wang, Slippery hydrogel with desiccation-tolerant 'skin' for high-precision additive manufacturing, Int. J. Extrem. Manuf. 6 (2024) 025501, https://doi.org/10.1088/2631-7990/ad1730.
[35] Y. Wang, J. Niu, J. Hou, Z. Wang, J. Wu, G. Meng, Z. Liu, X. Guo, A novel design strategy for triple-network structure hydrogels with high-strength, tough and self-healing properties, Polymer 135 (2018) 16–24, https://doi.org/10.1016/j.polymer.2017.11.076.
[36] L.B. Bezek, M.P. Cauchi, R. De Vita, J.R. Foerst, C.B. Williams, 3D printing tissue-mimicking materials for realistic transseptal puncture models, J. Mech. Behav. Biomed. Mater. 110 (2020) 103971, https://doi.org/10.1016/j.jmbbm.2020.103971.
[37] H. Gharib, Fine-needle aspiration biopsy of the thyroid: an appraisal, Ann. Intern. Med. 118 (1993) 282, https://doi.org/10.7326/0003-4819-118-4-199302150-00007.
[38] S. Sharma, R. Aguilera, J. Rao, J.K. Gimzewski, Piezoelectric needle sensor reveals mechanical heterogeneity in human thyroid tissue lesions, Sci. Rep. 9 (2019) 9282, https://doi.org/10.1038/s41598-019-45730-x.
[39] X. Bao, W. Li, M. Lu, Z.R. Zhou, Experiment study on puncture force between MIS suture needle and soft tissue, Biosurf. Biotribol. 2 (2016) 49–58, https://doi.org/10.1016/j.bsbt.2016.05.001.